Kekulé valence bond order in the honeycomb lattice optical Su-Schrieffer-Heeger model and its relevance to graphene

Sohan Malkaruge Costa,[1,2] Benjamin Cohen-Stead,[3,4] and Steven Johnston[3,5]

[1] *Department of Physics and Astronomy, The University of Tennessee, Knoxville, Tennessee 37996, USA*
[2] *Institute of Advanced Materials and Manufacturing, The University of Tennessee, Knoxville, Tennessee 37996, USA*
[3] *Department of Physics and Astronomy, The University of Tennessee, Knoxville, TN 37996, USA*
[4] *Institute of Advanced Materials and Manufacturing, The University of Tennessee, Knoxville, TN 37996, USA*
[5] *Institute for Advanced Materials and Manufacturing, The University of Tennessee, Knoxville, TN 37996, USA*

(Dated: September 17, 2024)

We perform sign-problem-free determinant quantum Monte Carlo simulations of the optical Su-Schrieffer-Heeger model on a half-filled honeycomb lattice. In particular, we investigate the model's semi-metal (SM) to Kekulé Valence Bond Solid (KVBS) phase transition at zero and finite temperatures as a function of phonon energy and interaction strength. Using hybrid Monte Carlo sampling methods we can simulate the model near the adiabatic regime, allowing us to access regions of parameter space relevant to graphene. Our simulations suggest that the SM-KVBS transition is weakly first-order at all temperatures, with graphene situated close to the phase boundary in the SM region of the phase diagram. Our results highlight the important role bond-stretching phonon modes play in the formation of KVBS order in strained graphene-derived systems.

Introduction — Graphene has undergone extensive investigation since it was first isolated [1, 2]. The low-energy physics of undoped monolayer graphene is characterized by a pair of inequivalent gapless Dirac cones located at the edge of the first Brillouin zone [3]. This electronic structure, together with its two-dimensional character, gives rise to a host of exotic emergent properties, including massless Dirac fermion physics, ballistic transport properties [4], the half-integer quantum Hall effect [5], and relativistic Klein tunneling [6].

Graphene's remarkable properties have tremendous potential for applications, which has motivated extensive studies on how they can be manipulated, e.g., through the application of strain [7] or in moiré systems [8, 9]. An important emergent property in this context is the formation of an insulating Kekulé Valence Bond Solid (KVBS) phase [7]. This state preserves time-reversal symmetry but gaps the Dirac cones while folding them back to the Γ point. It is also linked to chiral symmetry breaking [10, 11], charge fractionalization [12] and other electron and phonon related topological properties [13–16]. Theoretical and numerical results show that the KVBS state is not only allowed by symmetry [17] but can be stabilized by applied isotropic strain [18]. Experiments have observed KVBS correlations in a variety of settings, including graphene monolayers on silicon oxide [19] or copper [11] substrates, in lithium or calcium intercalated multi-layers [10, 20, 21], and with lithium adatom deposition [22, 23]. The semi-metal (SM) to insulating KVBS phase transition has also been of great fundamental interest. While Landau mean-field theory predicts a first-order transition at the corresponding quantum critical point (QCP), quantum fluctuations associated with coupling to gapless Dirac fermion modes can render the quantum phase transition second-order in the chiral XY universality class [24–26]. In contrast, the finite-temperature transition is expected to remain first-order [27].

The theoretical studies mentioned above have primarily focused on models dominated by electronic correlations. However, theoretical studies examining static lattice distortions on interacting honeycomb lattices have demonstrated their potential to impact the phase diagram [28, 29]. Similarly, a host of experimental, *ab initio*, and mean-field studies have shown that KVBS correlations are often accompanied by periodic lattice distortions and could be driven by electron-phonon (e-ph) coupling to graphene's optical in-plane bond-stretching modes [30–32]. This interaction results from the modulation of the hopping amplitudes, and it has been proposed as a potential pairing mechanism in twisted bilayer graphene [33, 34]. Nevertheless, its role in establishing the KVBS phase has yet to be firmly established as previous quantum Monte Carlo (QMC) studies of e-ph interactions have focused on Holstein models with high-energy phonons [35–37].

In this paper, we investigate the SM-KVBS transition in the optical Su-Schrieffer-Heeger (oSSH) model on a honeycomb lattice, where the in-plane atomic motion modulates the nearest-neighbor hopping amplitude [38, 39]. By performing sign-problem-free determinant quantum Monte Carlo (DQMC) simulations, we extract the model's ground-state and finite temperature phase diagrams as a function of phonon frequency and e-ph coupling strength while fully accounting for the quantum nature of the phonons. Our results suggest the SM-KVBS transition is a weakly first-order phase transition down to the QCP. Importantly, we can simulate parameters directly relevant to graphene, allowing us to situate this material close to the KVBS phase boundary. Our results indicate that e-ph interactions play a crucial role in forming the KVBS phase in strained graphene and help pave the way toward intentional strain engineering of the electronic properties of graphene-derived systems.

Model — Our model's Hamiltonian is $H = H_e + H_{\text{ph.}} + H_{e\text{-ph.}}$. The first term

$$H_e = -t \sum_{\mathbf{i},\nu,\sigma} \left[\hat{c}^\dagger_{\text{B},\mathbf{i},\sigma} \hat{c}_{\text{A},\mathbf{i}+\mathbf{r}_\nu,\sigma} + \text{h.c.} \right] - \mu \sum_{\mathbf{i},\gamma,\sigma} \hat{c}^\dagger_{\gamma,\mathbf{i},\sigma} \hat{c}_{\gamma,\mathbf{i},\sigma} \quad (1)$$

is the non-interacting electron tight-binding Hamiltonian, where the operator $\hat{c}^\dagger_{\gamma,\mathbf{i},\sigma}$, ($\hat{c}_{\gamma,\mathbf{i},\sigma}$) creates (annihilates) a spin-σ electron in orbital $\gamma \in \{\text{A}, \text{B}\}$ of unit cell $\mathbf{i}$. The parameter t specifies the nearest-neighbor hopping amplitude, setting the energy scale in the system, and μ is the chemical potential. Throughout, we consider a half-filled particle-hole symmetric system ($\mu = 0$), where the Fermi surface (FS) consists of a pair of Dirac points located at $\mathbf{K}_\pm = \frac{2\pi}{a}\left(\frac{1}{3}, \pm\frac{1}{3\sqrt{3}}\right)$.

The second term in H is the non-interacting lattice Hamiltonian

$$H_{\text{ph.}} = \sum_{\mathbf{i},\gamma} \left[\frac{1}{2M} \hat{P}^2_{\mathbf{i},\gamma} + \frac{1}{2} M \Omega^2 \hat{R}^2_{\mathbf{i},\gamma} \right]. \quad (2)$$

Here two optical phonon modes are placed on each site to describe the in-plane motion of the ions in the x- and y-directions, each with frequency Ω and ion mass M. The associated displacement and momentum operators are $\hat{\mathbf{R}}_{\mathbf{i},\gamma} = \left(\hat{X}_{\mathbf{i},\gamma}, \hat{Y}_{\mathbf{i},\gamma}\right)$ and $\hat{\mathbf{P}}_{\mathbf{i},\gamma} = \left(\hat{P}_{\mathbf{i},\gamma,X}, \hat{P}_{\mathbf{i},\gamma,Y}\right)$, respectively, with $\hat{R}^2_{\mathbf{i},\gamma} = |\hat{\mathbf{R}}_{\mathbf{i},\gamma}|^2$ and $\hat{P}^2_{\mathbf{i},\gamma} = |\hat{\mathbf{P}}_{\mathbf{i},\gamma}|^2$.

Finally, the third term in H describes the e-ph coupling

$$H_{e\text{-ph.}} = \alpha \sum_{\mathbf{i},\nu,\sigma} \Delta\hat{R}_{\mathbf{i},\nu} \left[\hat{c}^\dagger_{\text{B},\mathbf{i}+\mathbf{r}_\nu,\sigma} \hat{c}_{\text{A},\mathbf{i},\sigma} + \text{h.c.} \right], \quad (3)$$

where $\Delta\hat{R}_{\mathbf{i},\nu} = \left(\hat{\mathbf{R}}_{\mathbf{i}+\mathbf{r}_\nu,\text{B}} - \hat{\mathbf{R}}_{\mathbf{i},\text{A}}\right) \cdot \mathbf{r}_\nu / |\mathbf{r}_\nu|$ and $\mathbf{r}_\nu$ are the three nearest-neighbor vectors shown in Fig. 1(a). Here, the interaction arises from the linear modulation of the hopping amplitude with the change in bond length, projected onto the equilibrium bond direction $\Delta\hat{R}_{\mathbf{i},\nu}$. The parameter α controls the coupling strength. Throughout, we define the dimensionless ratio $\lambda = \alpha^2/(M\Omega^2 t)$ as a measure of dimensionless coupling, and normalize the mass to $M = 1$ [38].

Methods — We solve our model using DQMC with hybrid Monte Carlo (HMC) updates [40–44], as implemented in the `SmoQyDQMC.jl` package [45, 46]. Throughout, we consider clusters with a linear size L with $N = 2L^2$ orbitals and periodic boundary conditions (see Appendix A for additional details).

The KVBS state breaks a $\mathbb{Z}_3$ symmetry and has an electronic order parameter [25, 47]

$$\hat{\Psi}_e(\mathbf{K}) = \frac{1}{L^2} \sum_{\mathbf{i},\nu} \left[e^{-i\mathbf{K}\cdot\mathbf{i}} e^{i2\pi\nu/3} \hat{B}_{\mathbf{i},\nu} \right], \quad (4)$$

where $\mathbf{K} = \mathbf{K}_+ - \mathbf{K}_-$ is the scattering vector between the Dirac points, and $\hat{B}_{\mathbf{i},\nu} = \sum_\sigma (\hat{c}^\dagger_{\text{B},\mathbf{i}+\mathbf{r}_\nu,\sigma} \hat{c}_{\text{A},\mathbf{i},\sigma} + \text{h.c.})$ is the bond operator. An alternative order parameter can be defined using the lattice displacements

$$\hat{\Psi}_{\text{ph.}}(\mathbf{K}) = -\frac{1}{L^2} \sum_{\mathbf{i},\nu} \left[e^{-i\mathbf{K}\cdot\mathbf{i}} e^{i2\pi\nu/3} \Delta\hat{R}_{\mathbf{i},\nu} \right], \quad (5)$$

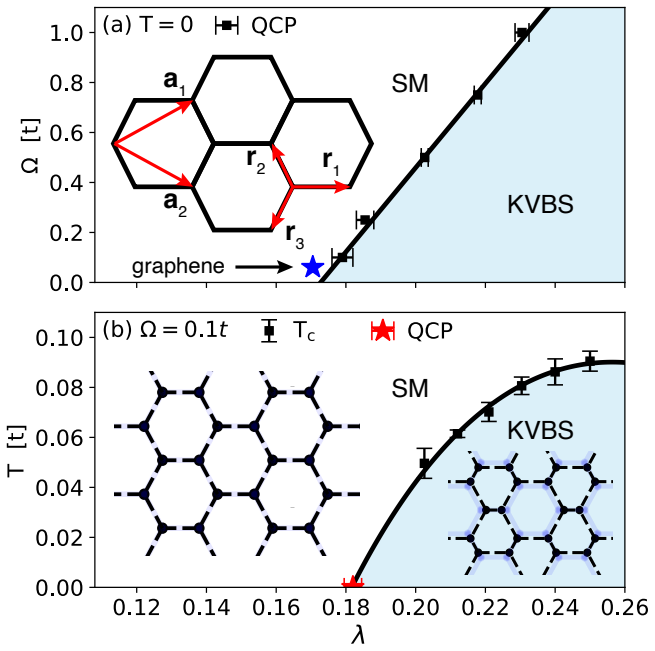

FIG. 1. (a) Zero- and (b) finite-temperature phase diagrams for the half-filled oSSH honeycomb model. The left inset in panel a) shows our convention for defining the unit cell. The left and right insets of panel b) show an undistorted honeycomb lattice and the KVBS lattice distortion pattern, respectively. The black markers in a) indicate the location of the QCP as a function of e-ph coupling λ and phonon energy Ω. The blue marker is the approximate location of graphene in this zero-temperature phase diagram. The black markers in panel b) are the T_c values obtained for $\Omega = 0.1t$ using the correlation ratio method. The red marker indicates the corresponding QCP. The black curves in both panels are guides for the eye.

which is sensitive to the distortion pictured in Fig. 1(b). The correspondence between $\hat{\Psi}_e(\mathbf{K})$ and $\hat{\Psi}_{\text{ph.}}(\mathbf{K})$ occurs because $\hat{B}_{\mathbf{i},\nu} \sim -\Delta\hat{R}_{\mathbf{i},\nu}$ in the model.

To detect the KVBS state, we measure the bond structure factor $S_{\text{vbs}}(\mathbf{K}) = L^2 \langle |\hat{\Psi}_e(\mathbf{K})|^2 \rangle$ and corresponding correlation ratio $R_{\text{vbs}}(\mathbf{K}) = 1 - S_{\text{vbs}}(\mathbf{K} + \delta\mathbf{q})/S_{\text{vbs}}(\mathbf{K})$, where $\mathbf{K} + \delta\mathbf{q}$ denotes the nearest momentum points to $\mathbf{K}$ for a given lattice size L. In the SM phase, $S_{\text{vbs}}(\mathbf{k})$ is relatively flat and $R_{\text{vbs}}(\mathbf{K}) \to 0$. Conversely, the bond structure factor will become peaked at $\mathbf{K}$ as KVBS correlations set in such that $R_{\text{vbs}}(\mathbf{K}) \to 1$ below the critical temperature and in the thermodynamic limit.

Phase Diagram — Figure 1 shows the zero- and finite-T phase diagrams of the half-filled oSSH model on a honeycomb lattice, which are our main results. In both cases, we see the emergence of a KVBS state from a SM phase, with no indication of additional antiferromagentic (AFM), charge-density-wave, or superconducting orders (see Appendix F).

Figure 1(a) plots the model's ground-state ($T = 0$) λ-

Ω phase diagram. The KVBS phase is characterized by both electronic bond correlations and a static periodic distortion of the lattice, pictured in the right inset of panel (b). These Kekulé lattice distortions are strongest in the adiabatic limit ($\Omega \to 0$) and correspond to the "Kek-O" phase characterized by a $\sqrt{3} \times \sqrt{3}$ supercell in which a central hexagon isotropically expands while the six adjacent hexagons contract via an alternating pattern of expanded and contracted bonds. Increasing Ω enhances quantum fluctuations of the lattice, which disrupt the pattern of Kekulé lattice distortions and shift the SM-KVBS phase boundary to larger λ.

The star in Fig. 1(a) indicates the approximate parameters corresponding to graphene. The relevant phonon modes in graphene are the A_1 and B_1 modes with energy $\Omega \approx 170$ meV $\approx 0.065t$ [33, 48, 49]. The lattice distortions associated with the A_1 phonon mode are consistent with the KVBS state, and couple to the electrons by modulating the nearest-neighbor hopping amplitude. We estimate the strength of this coupling as $\alpha \approx 6.09$ eV/Å with a corresponding $\lambda \approx 0.17$ (see Appendix B). As expected, monolayer graphene falls in the SM region of the phase diagram but lies very close to the SM-KVBS phase boundary. Thus, small perturbations that increase λ, as may be expected to accompany the application of an isotropic strain, could drive the emergence of a KVBS state [18].

Figure 1(b) shows the model's λ-T phase diagram for fixed phonon energy $\Omega = 0.1t$, where a phase transition to the KVBS state appears above a critical coupling λ_c. Previous investigations of this phase transition in purely electronic models indicate that it is weakly first-order at finite temperature but becomes second-order at the QCP, with the quantum phase transition being in the chiral XY universality class. Our results are consistent with a weakly first-order finite temperature transition in the oSSH model. However, they suggest that the transition remains weakly first-order down to $T = 0$ instead of becoming second-order at the QCP.

We first consider the finite temperature transition. Since this transition is expected to be weakly first-order [25, 50], we used several approaches to probe its character and determine the critical temperature T_c. Figure 2 presents a finite-size scaling (FSS) analysis of both the structure factor $S_{\text{vbs}}(\mathbf{K})$ and correlation ratio $R_{\text{vbs}}(\mathbf{K})$ for $\Omega = 0.1t$ and $\lambda = 0.25$. Formally, these kinds of FSS analyses are only valid for continuous phase transitions; however, for weakly first-order phase transitions, one can obtain a pseudo-scaling behavior for exponents different from the expected universality class but with the correct T_c [51]. The crossing point of $R_{\text{vbs}}(\mathbf{K})$ in Fig. 2(a) aligns with the one for $S_{\text{vbs}}(\mathbf{K})$ shown in Fig. 2(b). The inset in Fig. 2(b) shows the corresponding collapse, where the critical exponents $\beta \approx 0.46$ and $\nu \approx 0.76$, with an estimated transition temperature of $T_c/t \approx 1/11$. Given the broken $\mathbb{Z}_3$ symmetry of the KVBS state, these values differ from the three-state Potts model exponents ($\beta = 1/9$ and $\nu = 5/6$) we would expect if the transition were continuous. The transition temperature for other values of λ reported in Fig. 1(b) was determined using the crossing point for the correlation ratio given $L = 6$, 9, and 12.

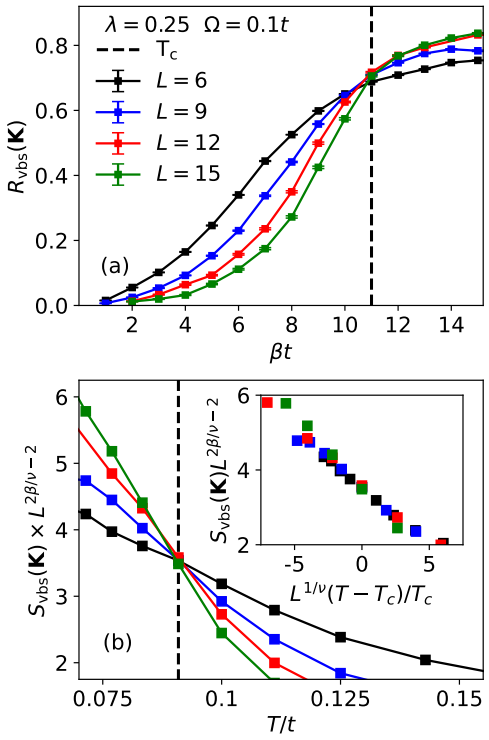

FIG. 2. Representative analyses of the finite-temperature SM-KVBS phase transition. a) The inverse temperature evolution of the $R_{\text{vbs}}(\mathbf{K})$ for different system sizes and $\lambda = 0.25$ and $\Omega = 0.1t$. The correlation ratio crossing point is approximately $T_c/t \approx 1/11$, as indicated by the black dashed lines. b) The scaled crossing of $S_{\text{vbs}}(\mathbf{K})$ versus temperature T using the critical exponents $\beta \approx 0.46$ and $\nu \approx 0.76$, based on the collapse shown in the inset.

To further probe the $\mathbb{Z}_3$ symmetry breaking and provide additional evidence suggesting a weakly first-order finite temperature transition, Fig. 3 displays histograms of sampled values of the lattice order parameter $\hat{\Psi}_{\text{ph.}}(\mathbf{K})$ for $\Omega = 0.1t$ and $\lambda = 0.22$ for an $L = 6$ lattice. At $\beta t = 1$ [Fig. 3(a)], well above the transition temperature and absent any symmetry breaking, the sampled $\hat{\Psi}_{\text{ph.}}(\mathbf{K})$ are symmetrically centered around zero. At $\beta t = 12$ [Fig. 3(b)], a temperature near the transition, a ring forms around the origin that is not perfectly radially symmetric. There is also significant weight persisting inside the ring, indicative of the fluctuating first-order nature of the KVBS correlations near T_c. At $\beta t = 22$ [Fig. 3(c)], well below the transition temperature, there is no residual weight near zero and three distinct hot spots have formed on the ring, a result of a broken $\mathbb{Z}_3$ symmetry. Additionally, the location of these three hot spots is consistent with lattice distortions associated with the KVBS state. This behavior is also quite evident in the radial density profiles $\rho_{\text{ph.}}(\mathbf{K})$ shown in Figs. 3(d)-(f), which are derived from the histograms shown in panels

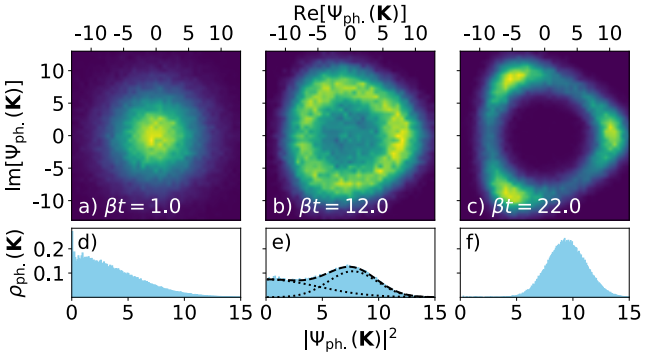

FIG. 3. The evolution of the distribution of $\Psi_{\text{lat.}}(\mathbf{K})$ across the SM to KVBS transition. The results are obtained for $L = 6, \Omega = 0.1t, \lambda = 0.22$ simulations. The top row shows results as a 2D histogram for $\text{Im}[\Psi_{\text{lat.}}(\mathbf{K})]$ vs $\text{Re}[\Psi_{\text{lat.}}(\mathbf{K})]$. The simulation in the SM phase (panel a) has a central peak. Simulations at the border of the SM-KVBS phase transition (panel b), develop a ring-like structure. Simulations in the KVBS phase (panel c) develop a three-lobe structure. The bottom row shows the radial distribution $\rho_{\text{lat.}}(\mathbf{K})$ at the same β values. A clear double-peak structure is evident at the boundary between the SM and KVBS phases (panel e), indicating the coexistence of two states and a first-order phase transition. The dotted lines show the two Gaussian lineshapes fitted to the double-peak structure, and the dashed line shows the complete fitting.

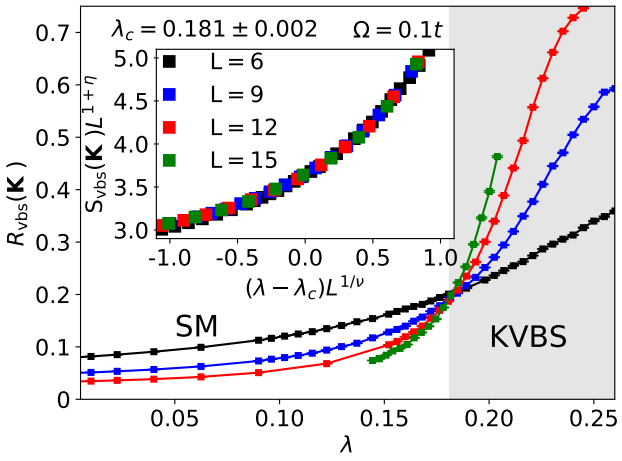

FIG. 4. A representative scaling analysis used to obtain the QCP for KVBS order with $\Omega/t = 0.1$. Here we have considered four lattice sizes with $\beta t = L$, as indicated in the legend. The gray region indicates KVBS order with a critical coupling for the SM-KVBS phase transition of $\lambda_c = 0.181 \pm 0.002$. The inset shows the corresponding finite-size scaling collapse with exponents $\eta \approx -1.16$ and $\nu \approx 0.67$.

(a)-(c), respectively.

To determine the location of the QCP, we again perform a FSS using the correlation ratio $R_{\text{vbs}}(\mathbf{K})$, as shown in Fig. 4. Holding the phonon frequency Ω fixed, λ_c is given by the crossing point of $R_{\text{vbs}}(\mathbf{K})$ vs λ curves for different lattice sizes L. This FSS analysis is based on the emergent Lorentz symmetry in the vicinity of the QCP in which $R_{\text{vbs}}(\mathbf{K})$ depends on $(\lambda - \lambda_c)/L^{\nu}$ and L^z/β, where $z = 1$. Therefore, we fix $\beta t = L$ in this analysis [52, 53]. Based on the crossing point, we determine that the critical coupling is $\lambda_c = 0.181 \pm 0.002$. The inset then shows the collapse of $S_{\text{vbs}}(\mathbf{K})$ if we appropriately rescale the axis, treating the critical exponents β and ν as free parameters. We find the optimal collapse with $\eta \approx -1.16$ and $\nu \approx 0.67$, values that are inconsistent with the Chiral XY universality class [24, 25, 27]. Performing a similar collapse of $R_{\text{vbs}}(\mathbf{K})$ gives a consistent estimate for ν as well (see Appendix G). These observations suggest that the QCP may remain weakly first-order instead of becoming second-order, as observed in similar studies of purely electronic models. The QCP for other values of λ reported in Fig. 1(a) was determined using lattice sizes $L = 6$, 9, and 12.

Discussion — We have presented the ground-state and finite-temperature phase diagrams for the half-filled oSSH model on a honeycomb lattice, investigating the SM-KVBS phase transition. For fixed phonon energy Ω, we identify a critical coupling λ_c above which the ground-state transitions from a SM to the KVBS state. A finite-temperature phase transition to the KVBS state emerges above λ_c, with T_c increasing monotonically with λ. We then estimated the location of graphene in the ground-state phase diagram by assuming the nearest-neighbor electron hopping amplitude couples to the high-energy in-plane A_1 bond-stretching phonon mode. The corresponding phonon energy and coupling parameters place graphene in the SM region of the phase diagram, but close to the phase boundary. This result provides new insight into why small perturbations to graphene-derived systems that effectively increase λ, as is expected to accompany the application of isotropic strain, can drive the system into a KVBS state. This has interesting implications for how strain engineering can be used to tune the electronic properties of graphene-based systems.

Our results also suggest that both the ground-state and finite-temperature SM-KVBS phase transitions are weakly first-order, in agreement with Landau mean-field theory predictions. This result is in contrast with similar QMC investigations of the quantum phase transition in purely electronic models, where coupling to gapless Dirac fermion modes renders the QCP second-order, in the chiral XY universality class. We suspect that our results differ from previous studies as a result of retardation effects associated with the e-ph interaction, which suppresses quantum fluctuations and has been shown to result in QCPs becoming first-order in other situations as well [54–56]. For instance, a recent investigation similarly found that lattice fluctuations associated with introducing spin-phonon interactions to the honeycomb Heisenberg model drive the deconfined QCP separating the AFM and KVBS ground-states to be first-order [47].

This work focused on half-filling and absent electronic correlations. It would be interesting to introduce a local repulsive Hubbard interaction to study competition

between SM, KVBS, and AFM correlations, as the role of e-ph interactions in this scenario has only been treated at the mean-field level [32]. Another avenue would be to study potential pairing with doping, as prior investigations have found that doping a KVBS state led to superconductivity and pseudogap formation [26].

Acknowledgements — This work was supported by the U.S. Department of Energy, Office of Science, Office of Basic Energy Sciences, under Award Number DE-SC0022311. This research used resources of the Oak Ridge Leadership Computing Facility, a DOE Office of Science User Facility supported under Contract No. DE-AC05-00OR22725.

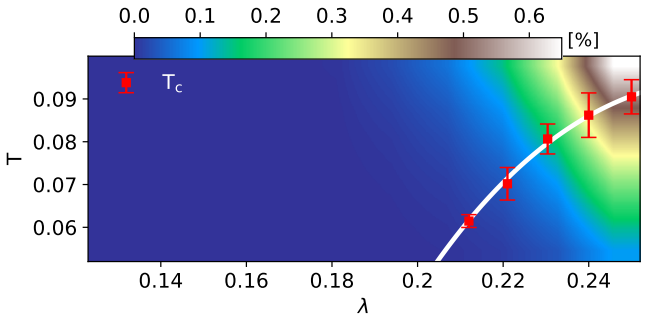

FIG. 5. A $\lambda - T$ heat map of the hopping inversion ratio η_{inv}, measured on an $L = 6$ cluster with $\Omega = 0.1t$. Markers and the red line indicate the boundary of the SM-KVBS phase transition. The heat map indicates the hopping inversion is lower than 1% of the total simulation updates. The top right corner shows the bright spot on the heat map, indicating a higher amount of phase inversion occurring in that region.

Appendix A: DQMC simulations

To obtain our results we ran simulations with 12 walkers in parallel, each performing $\sim 5,000$ HMC thermalization updates with $\sim 10,000$ HMC measurement updates. Throughout, we set the imaginary-time discretization to $\Delta\tau = 0.05$. Each HMC update was performed using $N_t \approx 4$ time-steps, with the step-size given by $\Delta t \approx \pi/(2\Omega N_t)$. Refer to Ref. [45] for more information regarding the details of the HMC algorithm.

Appendix B: Parameter estimates for graphene

The relevant phonon modes at the $\mathbf{K}_\pm$ Dirac points in graphene are associated with A_1 and B_1 phonon branches, with corresponding energies of $\hbar\Omega \approx 170$ meV [33, 48, 49]. The lattice distortions associated with the A_1 and B_1 phonons are consistent with the Kekulé lattice distortion pattern observed in our DQMC simulations. To estimate the coupling strength α, we

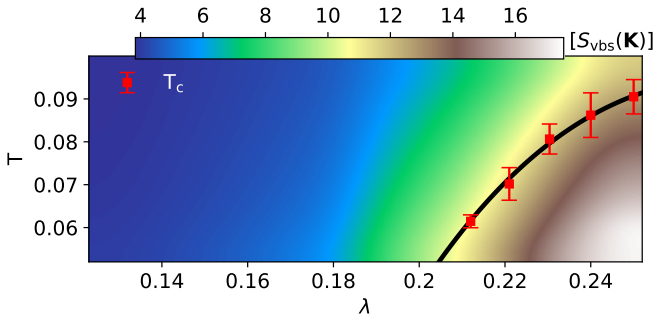

FIG. 6. A heat-map of the KVBS structure-factor $S_{\text{vbs}}(\mathbf{K})$ for $L = 6, \Omega = 0.1t$, with the black line approximating the location of the SM-KVBS phase boundary.

consider the functional form for the hopping amplitude,

$$t_{\text{eff}}(\Delta R) = te^{-\kappa\frac{\Delta R}{a}} \approx t - \alpha\Delta R + \mathcal{O}(\Delta R^2), \tag{B1}$$

which is commonly used in the literature for small changes in the equilibrium bond length ΔR. Here, $a = 1.41$ Å is the lattice parameter in the semi-metal phase, $t = 2.6$ eV, and $\kappa = 3.3$ [57]. Thus, the e-ph coupling strength in the linear approximation is $\alpha = \kappa t/a \approx 6.09$ eV/Å. The corresponding dimensionless coupling in our notation is

$$\lambda = \frac{\alpha^2}{M\Omega^2 t} = 0.17, \tag{B2}$$

where M is the mass of carbon and $\hbar\Omega/t = 0.065$.

Appendix C: Hopping inversion and Phase

In Su-Schrieffer-Heeger (SSH) models, phonon displacements modulate the nearest neighbor hopping amplitude. At linear order in the atomic displacements, the effective hopping is parameterized as in Eq. (B1) and can change sign for sufficiently large coupling strength α and lattice displacements ΔR. When this occurs, the sign of the effective hopping integral inverts, which induces significant changes in the model's ground- and excited-state properties [38, 58]. It is important to note that such sign changes are not physical but rather a byproduct of the linear approximation for the e-ph interaction (see Sec. B).

Our implementation of the DQMC algorithm does not place any restrictions on the phonon displacements, so it is possible for t_{eff} to be negative. To ensure this does not happen in our model, we measure what percentage of the time this occurs as

$$\eta_{\text{inv}} = 100 \times \langle \Theta(\alpha\hat{R}_{\mathbf{i},\nu} - t) \rangle, \tag{C1}$$

where Θ is the Heaviside function. Fig. 5 plots the evolution of this quantity as a function of temperature T and dimensionless coupling λ for our simulations performed on an $L = 6$ site cluster. The results indicate

that a hopping inversion rarely occurs (less than 0.5%) over the entire range of parameters, and that such inversions occur more frequently at high temperatures, where large thermal fluctuations form, or at strong e-ph coupling. Interestingly, the heat map shows that there is no direct relation between hopping inversion frequency and the formation of the KVBS phase.

Appendix D: Additional information on the SM-KVBS phase transition

The KVBS structure factor may be expressed as

$$\begin{aligned} S_{\rm vbs}(\mathbf{K}) =& L^2\ \langle|\hat{\Psi}_e(\mathbf{K})|^2\rangle = \sum_{\nu} S_B^{\nu,\nu}(\mathbf{K}) \\ &- \sum_{\nu<\nu'} \mathrm{Re}\Big[S_B^{\nu,\nu'}(\mathbf{K})\Big] \\ &- \sqrt{3}\sum_{\nu<\nu'} (-1)^{\nu+\nu'+1}\mathrm{Im}\Big[S_B^{\nu,\nu'}(\mathbf{K})\Big], \end{aligned} \tag{D1}$$

where

$$S_B^{\nu,\nu'} = \frac{1}{L^2}\sum_{\mathbf{i},\mathbf{r}} e^{-i\mathbf{K}\cdot\mathbf{r}}\langle \hat{B}_{\mathbf{i}+\mathbf{r},\nu}\hat{B}_{\mathbf{i},\nu'}\rangle \tag{D2}$$

is the equal-time bond-structure factor between bonds ν and ν', measured at the scattering momentum $\mathbf{K}$ connecting the two Dirac points. Fig. 6 plots a heat map $S_{\rm vbs}(\mathbf{K})$ for an $L = 6$ lattice with $\Omega = 0.1t$. The red line indicates the best fit line we obtain for transition temperature $T_{\rm c}$ of the SM-KVBS transition. The heat-map matches well with the estimated $T_{\rm c}$ values, with larger $S_{\rm vbs}(\mathbf{K})$ values appearing in the KVBS phase.

Appendix E: Results for the electron spectral function

Figure 7 provides additional results for the single-particle spectral function $A(\mathbf{k},\omega)$ as a function of phonon energy Ω and a fixed e-ph coupling $\lambda = 0.25$. For $\Omega = 0.1t$ (Fig. 7a), the system is in the KVBS phase and a gap forms in $A(\mathbf{k},\omega)$ at the Dirac point. As the phonon energy is increased, the size of the gap decreases for $\Omega = t/2$ (Fig. 7b) and ultimately closes for $\Omega = t$ (Fig. 7c). These results are in line with the theoretical prediction that this particular KVBS order ("Kek-O" order) induces a gap at the Dirac point.

Appendix F: Absence of competing charge-density-wave or antiferromagnetic correlations

Figure 8 shows results for the charge-density-wave (CDW), AFM, and KVBS structure factors at fixed $T = t/12$. The measurements show an absence of CDW and AFM phases for the given Ω range. The CDW and AFM structure factors are given by

$$S_{\rm cdw}(\mathbf{\Gamma}) = \frac{1}{N}\sum_{\mathbf{i},\mathbf{j}}\langle(\hat{n}_{A,\mathbf{i}} - \hat{n}_{B,\mathbf{i}})(\hat{n}_{A,\mathbf{j}} - \hat{n}_{B,\mathbf{j}})\rangle \tag{F1}$$

and

$$S_{\rm afm}(\mathbf{\Gamma}) = \frac{1}{N}\sum_{\mathbf{i},\mathbf{j}}\langle(\hat{S}^z_{A,\mathbf{i}} - \hat{S}^z_{B,\mathbf{i}})(\hat{S}^z_{A,\mathbf{j}} - \hat{S}^z_{B,\mathbf{j}})\rangle, \tag{F2}$$

respectively, where $\hat{n}_{\gamma,\mathbf{i}}$ and $\hat{S}^z_{\gamma,\mathbf{i}}$ are the total electron number and spin-z operators for orbital γ in unit cell $\mathbf{i}$. The definition of $S_{\rm vbs}(\mathbf{K})$ is provided in the main text.

Appendix G: Finite Size Scaling Collapse

Figure 9 shows the collapses of $R_{\rm vbs}(\mathbf{K})$ using two different values for the critical exponent ν. The left panel is for $\nu = 0.67$, which is the optimal value obtained based on the $S_{\rm vbs}(\mathbf{K})$ collapse reported in the main text. The panel on the right shows the collapse for $\nu = 1.05$, a value previously reported for the chiral XY universality class [24, 32]. The $\nu = 0.67$ results in a better collapse of the data compared to the $\nu = 1.05$ results.

[1] K. S. Novoselov, A. K. Geim, S. V. Morozov, D.-e. Jiang, Y. Zhang, S. V. Dubonos, I. V. Grigorieva, and A. A. Firsov, Electric field effect in atomically thin carbon films, science **306**, 666 (2004).

[2] K. S. Novoselov, A. K. Geim, S. V. Morozov, D. Jiang, M. I. Katsnelson, I. V. Grigorieva, S. V. Dubonos, and A. A. Firsov, Two-dimensional gas of massless dirac fermions in graphene, Nature **438**, 197 (2005).

[3] A. H. Castro Neto, F. Guinea, N. M. R. Peres, K. S. Novoselov, and A. K. Geim, The electronic properties of graphene, Rev. Mod. Phys. **81**, 109 (2009).

[4] X. Du, I. Skachko, A. Barker, and E. Y. Andrei, Approaching ballistic transport in suspended graphene, Nature Nanotechnology **3**, 491 (2008).

[5] Y. Zhang, Y.-W. Tan, H. L. Stormer, and P. Kim, Experimental observation of the quantum Hall effect and Berry's phase in graphene, Nature **438**, 201 (2005).

[6] C. W. J. Beenakker, Colloquium: Andreev reflection and Klein tunneling in graphene, Rev. Mod. Phys. **80**, 1337 (2008).

[7] G. G. Naumis, S. A. Herrera, S. P. Poudel, H. Nakamura, and S. Barraza-Lopez, Mechanical, electronic, optical, piezoelectric and ferroic properties of strained graphene and other strained monolayers and multilayers: an update, Rep. Prog. Phys **87**, 016502 (2023).

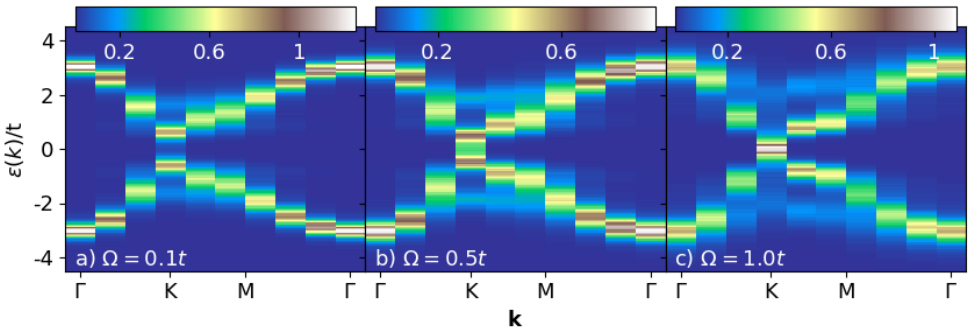

FIG. 7. The spectral function $A(\mathbf{k},\omega)$ for $L = 9$ lattice under $\lambda = 0.25$ for different phonon frequency Ω. For panel a) and b) the formation of a KVBS state results in a gap opening at the FS.

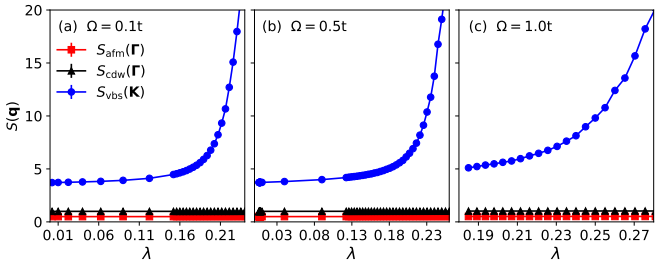

FIG. 8. The evolution of the AFM, CDW, and KVBS structure factors as a function of the e-ph coupling strength λ for fixed $T = t/12$. Results are shown for (a) $\Omega = 0.1t$, (b) $\Omega = 0.5t$, and $\Omega = t$. The expected ordering vector for the AFM and CDW correlations is $\mathbf{\Gamma} = (0,0)$ while the ordering vector $\mathbf{K}$ for the KVBS correlations is defined in the main text.

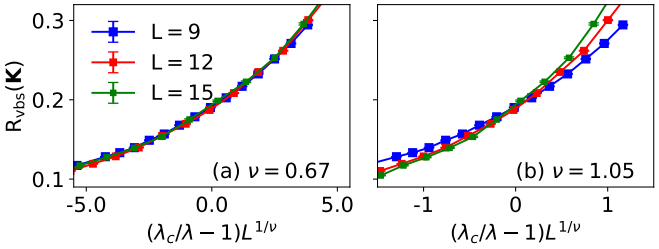

FIG. 9. The collapse of $R_{\rm vbs}(\mathbf{K})$ for different values of the critical exponent ν. Panel (a) shows that a better collapse can be obtained for $\nu = 0.67$ than panel (b), which uses the previously reported value $\nu = 1.05$ for the chiral XY universality class.

[8] Y. Cao, V. Fatemi, A. Demir, S. Fang, S. L. Tomarken, J. Y. Luo, J. D. Sanchez-Yamagishi, K. Watanabe, T. Taniguchi, E. Kaxiras, *et al.*, Correlated insulator behaviour at half-filling in magic-angle graphene superlattices, Nature **556**, 80 (2018).

[9] Y. Cao, V. Fatemi, S. Fang, K. Watanabe, T. Taniguchi, E. Kaxiras, and P. Jarillo-Herrero, Unconventional superconductivity in magic-angle graphene superlattices, Nature **556**, 43 (2018).

[10] C. Bao, H. Zhang, T. Zhang, X. Wu, L. Luo, S. Zhou, Q. Li, Y. Hou, W. Yao, L. Liu, P. Yu, J. Li, W. Duan, H. Yao, Y. Wang, and S. Zhou, Experimental evidence of chiral symmetry breaking in Kekulé-ordered graphene, Phys. Rev. Lett. **126**, 206804 (2021).

[11] C. Gutiérrez, C.-J. Kim, L. Brown, T. Schiros, D. Nordlund, E. B. Lochocki, K. M. Shen, J. Park, and A. N. Pasupathy, Imaging chiral symmetry breaking from Kekulé bond order in graphene, Nature Physics **12**, 950 (2016).

[12] C.-Y. Hou, C. Chamon, and C. Mudry, Electron fractionalization in two-dimensional graphenelike structures, Phys. Rev. Lett. **98**, 186809 (2007).

[13] Z. Lin, W. Qin, J. Zeng, W. Chen, P. Cui, J.-H. Cho, Z. Qiao, and Z. Zhang, Competing gap opening mechanisms of monolayer graphene and graphene nanoribbons on strong topological insulators, Nano letters **17**, 4013 (2017).

[14] L.-H. Wu and X. Hu, Topological properties of electrons in honeycomb lattice with detuned hopping energy, Scientific Reports **6**, 24347 (2016).

[15] A. Blason and M. Fabrizio, Local Kekulé distortion turns twisted bilayer graphene into topological Mott insulators and superconductors, Phys. Rev. B **106**, 235112 (2022).

[16] Y. Liu, C.-S. Lian, Y. Li, Y. Xu, and W. Duan, Pseudospins and topological effects of phonons in a Kekulé lattice, Phys. Rev. Lett. **119**, 255901 (2017).

[17] R. L. Frank and E. H. Lieb, Possible lattice distortions in the hubbard model for graphene, Phys. Rev. Lett. **107**, 066801 (2011).

[18] S. Sorella, K. Seki, O. O. Brovko, T. Shirakawa, S. Miyakoshi, S. Yunoki, and E. Tosatti, Correlation-driven dimerization and topological gap opening in isotropically strained graphene, Phys. Rev. Lett. **121**, 066402 (2018).

[19] D. Eom and J.-Y. Koo, Direct measurement of strain-driven Kekulé distortion in graphene and its electronic properties, Nanoscale **12**, 19604 (2020).

[20] K. Sugawara, K. Kanetani, T. Sato, and T. Takahashi, Fabrication of Li-intercalated bilayer graphene, Aip Advances **1** (2011).

[21] K. Kanetani, K. Sugawara, T. Sato, R. Shimizu, K. Iwaya, T. Hitosugi, and T. Takahashi, Ca intercalated bilayer graphene as a thinnest limit of superconducting C_6Ca, Proceedings of the National Academy of Sciences **109**, 19610 (2012).

[22] A. C. Qu, P. Nigge, S. Link, G. Levy, M. Michiardi, P. L. Spandar, T. Matthé, M. Schneider, S. Zhdanovich, U. Starke, *et al.*, Ubiquitous defect-induced density wave

instability in monolayer graphene, Science advances **8**, eabm5180 (2022).
[23] V. Cheianov, V. Fal'ko, O. Syljuåsen, and B. Altshuler, Hidden Kekulé ordering of adatoms on graphene, Solid State Communications **149**, 1499 (2009).
[24] Z.-X. Li, Y.-F. Jiang, S.-K. Jian, and H. Yao, Fermion-induced quantum critical points, Nature communications **8**, 314 (2017).
[25] X. Y. Xu, K. T. Law, and P. A. Lee, Kekulé valence bond order in an extended Hubbard model on the honeycomb lattice with possible applications to twisted bilayer graphene, Phys. Rev. B **98**, 121406 (2018).
[26] Z.-X. Li, S. G. Louie, and D.-H. Lee, Emergent superconductivity and non-fermi liquid transport in a doped valence bond solid insulator, Phys. Rev. B **107**, L041103 (2023).
[27] Y. Da Liao, Z. Y. Meng, and X. Y. Xu, Valence bond orders at charge neutrality in a possible two-orbital extended Hubbard model for twisted bilayer graphene, Phys. Rev. Lett. **123**, 157601 (2019).
[28] W. Wu, S. Rachel, W.-M. Liu, and K. Le Hur, Quantum spin Hall insulators with interactions and lattice anisotropy, Phys. Rev. B **85**, 205102 (2012).
[29] M. Bunney, T. Mizoguchi, Y. Hatsugai, and S. Rachel, Competition of first-order and second-order topology on the honeycomb lattice, Phys. Rev. B **105**, 045113 (2022).
[30] H. Zhang, C. Bao, M. Schüler, S. Zhou, Q. Li, L. Luo, W. Yao, Z. Wang, T. P. Devereaux, and S. Zhou, Self-energy dynamics and the mode-specific phonon threshold effect in Kekulé-ordered graphene, National Science Review **9**, nwab175 (2021).
[31] L. Classen, M. M. Scherer, and C. Honerkamp, Instabilities on graphene's honeycomb lattice with electron-phonon interactions, Phys. Rev. B **90**, 035122 (2014).
[32] Y. Otsuka and S. Yunoki, Kekulé valence bond order in the Hubbard model on the honeycomb lattice with possible lattice distortions for graphene, Phys. Rev. B **109**, 115131 (2024).
[33] F. Wu, A. H. MacDonald, and I. Martin, Theory of phonon-mediated superconductivity in twisted bilayer graphene, Phys. Rev. Lett. **121**, 257001 (2018).
[34] B. Lian, Z. Wang, and B. A. Bernevig, Twisted bilayer graphene: A phonon-driven superconductor, Phys. Rev. Lett. **122**, 257002 (2019).
[35] Y.-X. Zhang, W.-T. Chiu, N. C. Costa, G. G. Batrouni, and R. T. Scalettar, Charge order in the Holstein model on a honeycomb lattice, Phys. Rev. Lett. **122**, 077602 (2019).
[36] C. Chen, X. Y. Xu, Z. Y. Meng, and M. Hohenadler, Charge-density-wave transitions of Dirac fermions coupled to phonons, Phys. Rev. Lett. **122**, 077601 (2019).
[37] O. Bradley, B. Cohen-Stead, S. Johnston, K. Barros, and R. T. Scalettar, Charge order in the kagome lattice Holstein model: a hybrid Monte Carlo study, npj Quantum Materials **8**, 21 (2023).
[38] S. Malkaruge Costa, B. Cohen-Stead, A. Tanjaroon Ly, J. Neuhaus, and S. Johnston, Comparative determinant quantum monte carlo study of the acoustic and optical variants of the Su-Schrieffer-Heeger model, Phys. Rev. B **108**, 165138 (2023).
[39] A. Tanjaroon Ly, B. Cohen-Stead, S. Malkaruge Costa, and S. Johnston, Comparative study of the superconductivity in the holstein and optical Su-Schrieffer-Heeger models, Phys. Rev. B **108**, 184501 (2023).
[40] S. Beyl, F. Goth, and F. F. Assaad, Revisiting the hybrid quantum Monte Carlo method for Hubbard and electron-phonon models, Phys. Rev. B **97**, 085144 (2018).
[41] G. G. Batrouni and R. T. Scalettar, Langevin simulations of a long-range electron-phonon model, Phys. Rev. B **99**, 035114 (2019).
[42] B. Cohen-Stead, O. Bradley, C. Miles, G. Batrouni, R. Scalettar, and K. Barros, Fast and scalable quantum Monte Carlo simulations of electron-phonon models, Phys. Rev. E **105**, 065302 (2022).
[43] J. Ostmeyer, T. Nematiaram, A. Troisi, and P. Buividovich, First-principle quantum monte-carlo study of charge carrier mobility in organic molecular semiconductors, arXiv:2312.14914 (2023).
[44] J. Ostmeyer and P. Buividovich, Minimal autocorrelation in hybrid monte carlo simulations using exact fourier acceleration, arXiv:2404.09723 (2024).
[45] B. Cohen-Stead, S. M. Costa, J. Neuhaus, A. T. Ly, Y. Zhang, R. Scalettar, K. Barros, and S. Johnston, SmoQyDQMC.jl: A flexible implementation of determinant quantum Monte Carlo for Hubbard and electron-phonon interactions (2024).
[46] B. Cohen-Stead, S. M. Costa, J. Neuhaus, A. T. Ly, Y. Zhang, R. Scalettar, K. Barros, and S. Johnston, Codebase release r0.3 for SmoQyDQMC.jl, SciPost Phys. Codebases , 29 (2024).
[47] M. Weber, Valence bond order in a honeycomb antiferromagnet coupled to quantum phonons, Phys. Rev. B **103**, L041105 (2021).
[48] D. M. Basko, Effect of inelastic collisions on multiphonon Raman scattering in graphene, Phys. Rev. B **76**, 081405 (2007).
[49] D. M. Basko and I. L. Aleiner, Interplay of Coulomb and electron-phonon interactions in graphene, Phys. Rev. B **77**, 041409 (2008).
[50] Z. Zhou, D. Wang, Z. Y. Meng, Y. Wang, and C. Wu, Mott insulating states and quantum phase transitions of correlated SU($2N$) Dirac fermions, Phys. Rev. B **93**, 245157 (2016).
[51] S. Iino, S. Morita, N. Kawashima, and A. W. Sandvik, Detecting signals of weakly first-order phase transitions in two-dimensional Potts models, Journal of the Physical Society of Japan **88**, 034006 (2019).
[52] F. F. Assaad and I. F. Herbut, Pinning the order: The nature of quantum criticality in the Hubbard model on honeycomb lattice, Phys. Rev. X **3**, 031010 (2013).
[53] I. F. Herbut, V. Juričić, and B. Roy, Theory of interacting electrons on the honeycomb lattice, Phys. Rev. B **79**, 085116 (2009).
[54] S. Sarkar, L. Franke, N. Grivas, and M. Garst, Quantum criticality on a compressible lattice, Phys. Rev. B **108**, 235126 (2023).
[55] A. Samanta, E. Shimshoni, and D. Podolsky, Phonon-induced modification of quantum criticality, Phys. Rev. B **106**, 035154 (2022).
[56] P. Chandra, P. Coleman, M. A. Continentino, and G. G. Lonzarich, Quantum annealed criticality: A scaling description, Phys. Rev. Res. **2**, 043440 (2020).
[57] R. Ribeiro, V. M. Pereira, N. Peres, P. Briddon, and A. C. Neto, Strained graphene: tight-binding and density functional calculations, New Journal of Physics **11**, 115002 (2009).
[58] D. Banerjee, J. Thomas, A. Nocera, and S. Johnston, Ground-state and spectral properties of the doped

one-dimensional optical Hubbard-Su-Schrieffer-Heeger model, Phys. Rev. B **107**, 235113 (2023).